

Dynamics of Stellar Collisions

J. E. Barnes

*Institute for Astronomy, University of Hawaii, 2680 Woodlawn Drive,
Honolulu HI, 96822*

Abstract. I compare gas-dynamical and stellar-dynamical models of collisions. These two models have distinctly different physics; for example, shocks introduce irreversibility in gas systems, while stellar systems evolve in a completely reversible fashion. Nonetheless, both models yield broadly similar results, suggesting that analogies between gas and stellar dynamics have some heuristic validity even applied to collisions.

1. Introduction

Stars and galaxies are prototypical examples of self-gravitating systems. While both are held together by gravity, they differ in size, makeup, and structure. From a dynamical point of view, the basic difference is that stars are made up of particles which *often* undergo collisions, while galaxies are made up of particles which almost *never* collide (this conference notwithstanding).

Analogies between stellar and gaseous systems run deep. For example, there is a close relationship between spherical stellar systems with isotropic distribution functions $f = f(E)$ and gaseous systems with barotropic equations of state $P = P(\rho)$. The stability properties of spherical stellar and gaseous systems provide further analogies; an isotropic stellar system with $df/dE < 0$ is stable if the barotropic gas-sphere with the same density profile is stable (Antonov 1962; Lynden-Bell 1962). This is a sufficient but not necessary condition; on the whole, spherical stellar systems seem to be *more* stable than their gaseous counterparts. For flattened systems the situation is more complex. Infinite, uniformly rotating sheets of gas and stars have very similar stability criteria (Toomre 1964). On the other hand, certain finite, uniformly-rotating stellar disks (Kalnajs 1972) are much *less* stable than gaseous disks with the same density profile.

Questions of existence and stability exploit analogies between stellar and gaseous systems at or near equilibrium. In this paper I use numerical simulations to examine how such analogies work in situations which are far from equilibrium: collisions. Colliding stars and colliding spherical galaxies evolve in superficially similar ways, as seen in Fig. 1. Here the top row of frames shows a collision of two gas-spheres, while the bottom row shows the analogous collision of two spherical systems of collisionless particles, hereafter labeled “grit”¹. A more

¹In my original presentation I used “dust” instead of “grit”, borrowing this term from cosmology. However, S. Shapro pointed out that “dust” is only applicable to a cold, pressureless medium. Casting about for a suitable term, I chose “grit” since this conveys some resilience to pressure.

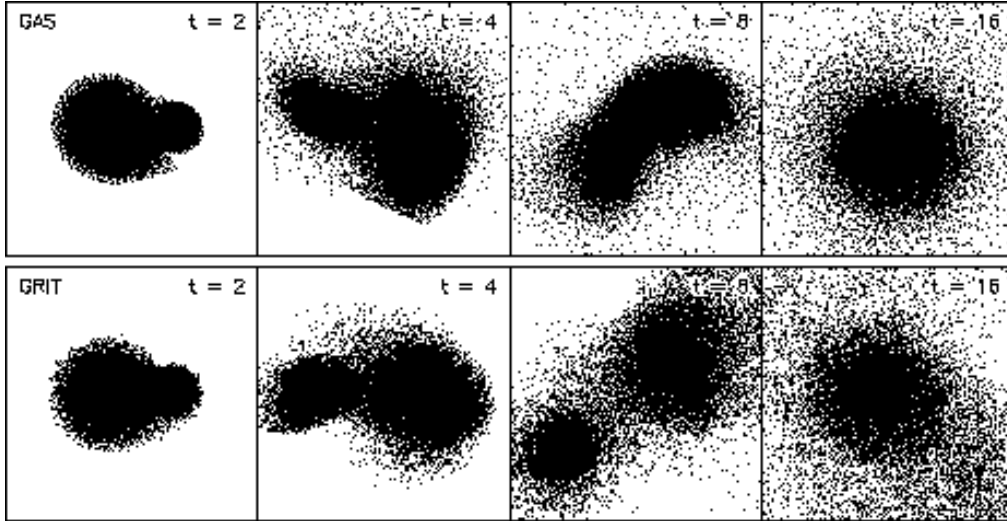


Figure 1. Gas (top) and grit (bottom) versions of the same collision. Initially the two bodies approach on a parabolic relative orbit, passing each other in a counter-clockwise direction. The mass ratio is $M_1/M_2 = 2$ and the targeted pericentric separation $r_p = 0.5$ is half the radius of the larger body.

detailed comparison of the two collisions in Fig. 1 reveals significant differences. For example, it's evident that orbit decay doesn't work in quite the same way; contrasting the third pair of frames, the two bodies are much closer in the gas model than they are in the grit model. Moreover, grit evolves *reversibly*, while gas evolves *irreversibly*; by integrating the merged grit model backward in time, one can unscramble the wreckage and recover the initial conditions (van Albada & van Gorkom 1977), but the presence of shocks in the gas model precludes such reversals.

1.1. Gas model

Technically, the interior of a normal star is a partly-ionized plasma in local equilibrium with a black-body radiation field; support against gravity is provided by some combination of thermal and radiation pressure. But for low-mass stars the latter is insignificant, and to a good approximation the pressure is given by the equation of state for an ideal gas.

Gas dynamics unfolds in a space of three dimensions; the dynamical variables are functions of position \mathbf{r} and time t . Two such variables are the density $\rho = \rho(\mathbf{r}, t)$ and the velocity field $\mathbf{v} = \mathbf{v}(\mathbf{r}, t)$. One more variable is needed to represent the thermodynamic state of the gas; in these calculations I use the entropy function $a = a(S)$, which enters directly in the equation of state:

$$P = a(S)\rho^\gamma, \quad (1)$$

where P is the pressure, and γ is the ratio of specific heats, here assigned the value $\gamma = 5/3$ appropriate for a monatomic gas.

I adopt the following dynamical equations:

$$\frac{\partial \rho}{\partial t} + \frac{\partial}{\partial \mathbf{r}} \cdot (\rho \mathbf{v}) = 0, \quad (2)$$

$$\frac{\partial \mathbf{v}}{\partial t} + \left(\mathbf{v} \cdot \frac{\partial}{\partial \mathbf{r}} \right) \mathbf{v} = -\frac{1}{\rho} \frac{\partial P}{\partial \mathbf{r}} - \frac{\partial \Phi}{\partial \mathbf{r}}, \quad (3)$$

$$\frac{\partial a}{\partial t} + \left(\mathbf{v} \cdot \frac{\partial}{\partial \mathbf{r}} \right) a = (\gamma - 1) \rho^{1-\gamma} \dot{u}_v. \quad (4)$$

Here eq. 2 represents conservation of mass and eq. 3 represents conservation of momentum; the gravitational potential Φ is calculated from Poisson's equation. Eq. 4 describes the evolution of the entropy function; the flow is adiabatic, conserving the entropy of each fluid element, except where the viscous heating function $\dot{u}_v > 0$. A standard form of artificial viscosity (Monaghan & Gingold 1983) is used to implement the increase in gas entropy due to shocks.

I solve these dynamical equations using Smoothed Particle Hydrodynamics or SPH (eg. Monaghan 1992). The code is similar to "TREESPH" (Hernquist & Katz 1989); it includes a hierarchical algorithm to compute gravitational forces, individual smoothing radii h_i set so that that each particle i interacts with a fixed number of neighbors, and individual time-steps adjusted to satisfy a Courant condition. The code doesn't include terms proportional to ∇h_i which arise when the SPH equations are derived from a Hamiltonian (Nelson & Papaloizou 1993, 1994). Since the code integrates Eq. 4 instead of the equivalent energy equation, the neglect of these ∇h_i terms leads to imperfect energy conservation (Hernquist 1993). Most of the calculations presented below conserve energy to $\sim 1\%$ or better, so the neglect of these terms is probably not critical in this application.

1.2. Grit model

The dominant mass components in typical galaxies are stars and dark matter. In the absence of conflicting evidence the latter is often assumed to be composed of particles with masses much less than $10^6 M_\odot$ (cf. Lacey & Ostriker 1985). The gravitational potential of a galaxy is quite smooth and individual stars or dark matter particles follow smooth trajectories, undisturbed by collisions, close encounters, or any effect due to the discrete nature of the mass.

Stellar dynamics unfolds in a space of six dimensions; the phase-space distribution $f = f(\mathbf{r}, \mathbf{v}, t)$ is a function of position \mathbf{r} , velocity \mathbf{v} , and time t . In the limit appropriate for galaxies, f evolves according to the Collisionless Boltzmann Equation or CBE:

$$\frac{\partial f}{\partial t} + \mathbf{v} \cdot \frac{\partial f}{\partial \mathbf{r}} - \frac{\partial \Phi}{\partial \mathbf{r}} \cdot \frac{\partial f}{\partial \mathbf{v}} = 0 \quad (5)$$

Like eq. 2, eq. 5 is a continuity equation, conserving the mass of the system. But eq. 5 describes an *incompressible* flow in six dimensions; dynamics moves elements of phase-fluid around but conserves the value of f associated with each.

I solve the CBE using standard N-body techniques (eg. Barnes 1998). The code uses a hierarchical algorithm to compute gravitational forces and a simple leap-frog integrator to advance particle coordinates.

1.3. Polytropes

I chose to collide simple polytropes, instead of using stellar models. While accurate simulations of merging stars require realistic stellar models (Sills & Lombardi 1997), polytropes are still appropriate for comparing the basic physics of stellar and galactic collisions. Polytropes are easily constructed, and their properties are well-understood (eg. Chandrasekhar 1939). Moreover, grit models of polytropes have simple distribution functions (Eddington 1916) and the stability of these systems has been studied using N-body simulations (Hénon 1973; Barnes, Goodman, & Hut 1986).

Both gas and grit polytropes obey the following relationship between mass density ρ and gravitational potential Φ :

$$\rho = \rho(\Phi) = \rho_1(1 - \Phi/\Phi_1)^n. \quad (6)$$

Here Φ_1 is the value of the potential on the surface of the polytrope and ρ_1 is a constant with units of density. By construction, gas polytropes are marginally stable to convection, and this implies that the index n is related to the ratio of specific heats by $n = 1/(\gamma - 1)$. For grit polytropes, n is a free parameter, and the distribution function takes the form

$$f = f(E) = \begin{cases} f_1(1 - E/\Phi_1)^{n-3/2} & \text{if } E < \Phi_1, \\ 0 & \text{otherwise,} \end{cases} \quad (7)$$

where f_1 is a constant with units of phase-space density.

For a monatomic gas, $\gamma = 5/3$, and the appropriate index $n = 3/2$. The corresponding grit polytrope has an unusually simple structure; f has the constant value f_1 within the six-dimensional volume defined by $E = \frac{1}{2}v^2 + \Phi(r) < \Phi_1$, and vanishes everywhere else.

To construct realizations of polytropes I first tabulated the density profile $\rho(r)$, potential $\Phi(r)$, and pressure $P(r)$. Grit models were generated by choosing initial positions \mathbf{r}_i and velocities \mathbf{v}_i for each particle according to the distribution function $f(\mathbf{r}, \mathbf{v}) = f(\frac{1}{2}v^2 + \Phi(r))$ (Hénon 1973). Likewise, gas models were generated by choosing initial positions \mathbf{r}_i according to the density profile $\rho(r)$, setting initial velocities $\mathbf{v}_i = 0$, and assigning initial entropy function values $a_i = P(r_i)/\rho^\gamma(r_i)$. In both cases all particles had equal masses. Since particle coordinates were assigned independently, these initial configuration have Poissonian fluctuations. Such fluctuations are inevitable in N-body simulations, but they are much larger than the fluctuations normally present in SPH calculations. Therefore, the gas realizations were relaxed by evolving them with the SPH code using a velocity-damping term. This has the effect of “ironing out” the initial density fluctuations without disturbing the overall density profile.

2. Collision Sample

The dynamics of a collision depend on the relative orbit and mass ratio of the participants as well as their internal structures. The collisions reported here were restricted to parabolic (zero-energy) orbits, which are appropriate for collisions in globular clusters and similar environments. I used $n = 3/2$ polytropes and assumed a linear relationship between mass and radius; these choices roughly

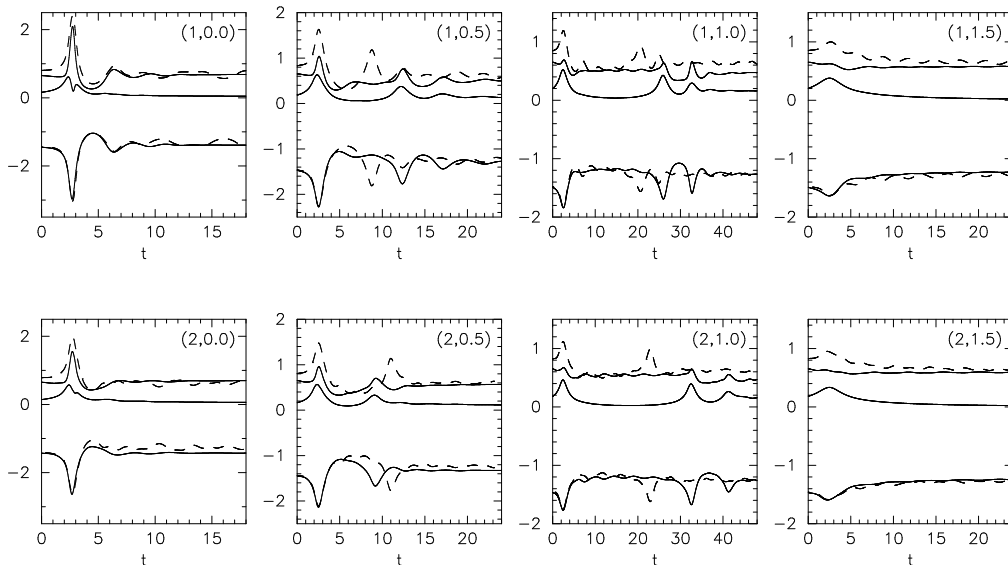


Figure 2. Energies vs. time for all collisions, each labeled by $(M_1/M_2, r_p)$. The three solid curves in each panel are from the gas models; from top to bottom, they show the thermal energy $T(t)$, kinetic energy $K(t)$, and potential energy $U(t)$. Likewise, the two dashed curves are from the grit models; they show the kinetic and potential energies.

caricature the properties of low-mass main-sequence stars. It may ultimately be worth relaxing these restrictions, but even with them in place, two parameters must still be chosen for each collision: the mass ratio and the pericentric separation of the initial relative orbit. I adopted mass ratios $M_1/M_2 = 1$ and 2, and studied collisions with pericentric separations r_p ranging from zero (head on) to $R_1 + R_2$ (grazing). To simplify comparisons between collisions with different mass ratios, I stipulated that all cases have the same total mass.

Since G is the only dimensional constant in these calculations, it's convenient to adopt units with $G = 1$. The polytropes used for the equal-mass collisions ($M_1/M_2 = 1$) have masses $M_1 = M_2 = 0.75$ mass units and radii $R_1 = R_2 = 0.75$ length units; for the gas models, the initial entropy function value is $a(S_1) = a(S_2) = 0.2889$. The polytropes used for the unequal-mass collisions ($M_1/M_2 = 2$) have masses $M_1 = 1.0$ and $M_2 = 0.5$ and radii $R_1 = 1.0$ and $R_2 = 0.5$; the initial entropy function values are $a(S_1) = 0.4240$ and $a(S_2) = 0.1682$.

For both mass ratios I considered four collisions with pericentric separations $r_p = 0, 0.5, 1, \text{ and } 1.5 (= R_1 + R_2)$; each collision was run with both gas and grit models, using 24576 particles for each calculation. I ran all collisions with $r_p \leq 1$ until the participants merged and relaxed to near-equilibrium configurations. The grazing collisions were not run to completion; orbit decay is very gradual in such wide passages and the time required to reach merger seemed excessive.

Fig. 2 summarizes the evolution of the collisions. In each case the participants have a first pericentric passage at $t \simeq 2.5$, marked by sharp minima in the

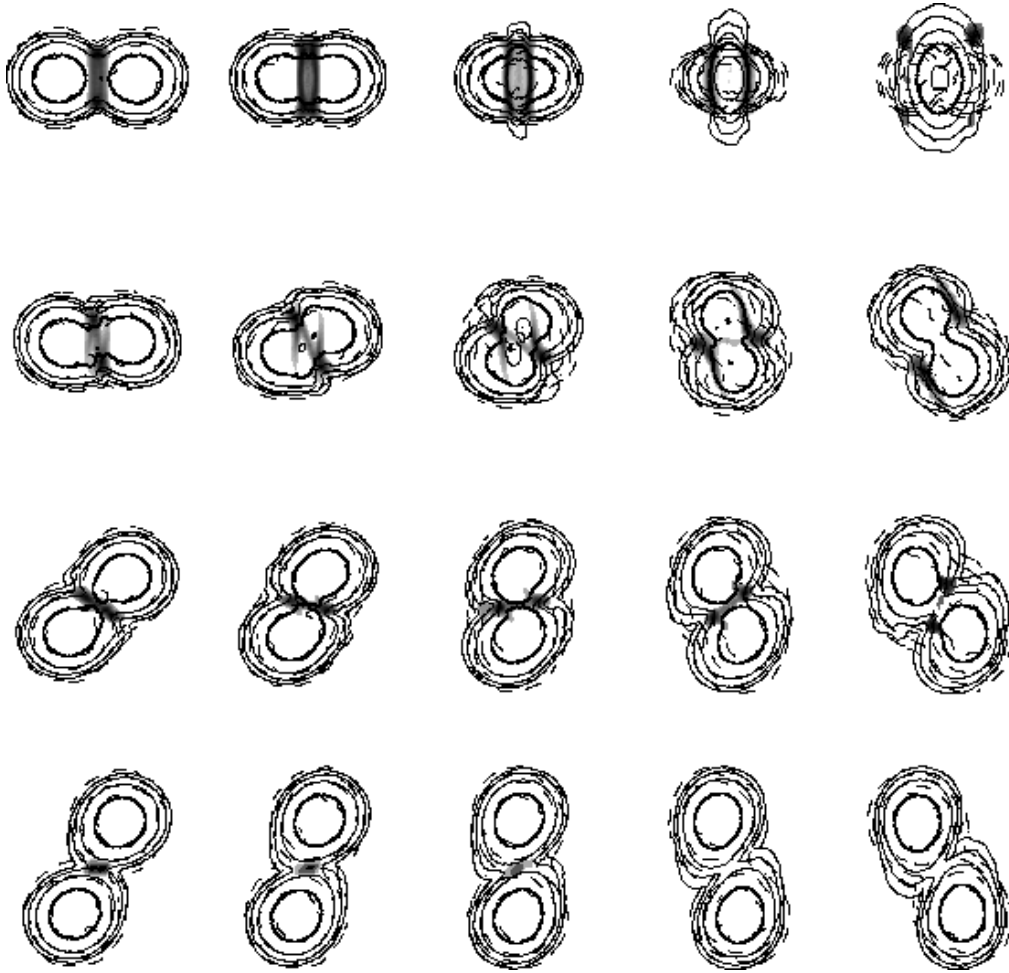


Figure 3. First passages for equal-mass collisions. Each row shows a different collision at times equally spaced between $t = 2$ and $t = 3$; r_p increases from top to bottom. Contours indicate density on the orbital plane in steps of a factor of 4; dashed lines show grit, solid lines show gas, with a heavier contour for $\rho = 1$. Half-tones indicate shocks.

curves of potential energies $U(t)$. In the grit models (dashed lines) this potential energy is entirely invested in kinetic energy $K(t)$, which has a maxima opposing the minima of $U(t)$. In the gas models (solid lines) the gravitational energy is shared between $K(t)$ and the thermal energy $T(t)$, with the relative apportionment depending on the collision parameters. Head-on collisions produce sharp peaks in $T(t)$ as gravitational energy heats the gas; the stored thermal energy drives a subsequent re-expansion and bounce before the system settles down. On the other hand, the collisions with $r_p \geq 1$ put most of the available gravitational energy into bulk motion, producing modest peaks in $K(t)$ while barely disturbing $T(t)$.

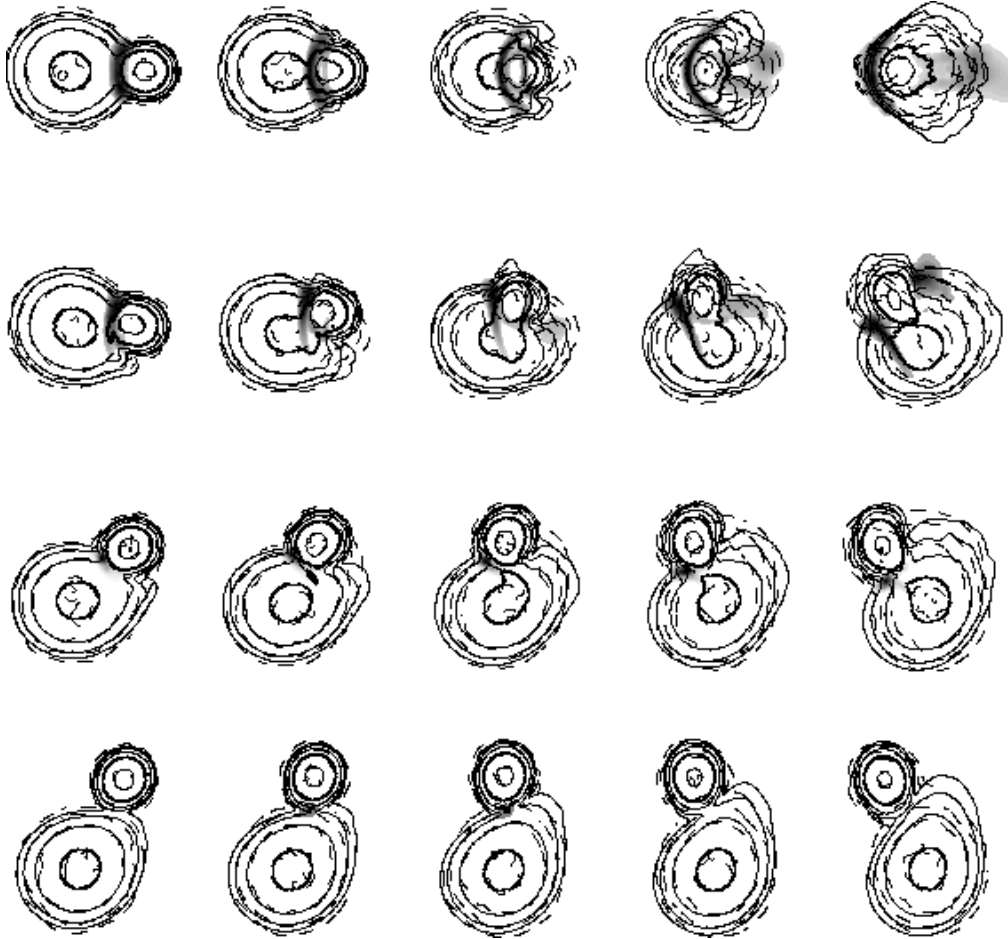


Figure 4. First passages for unequal-mass collisions. Each row shows a different collision at times equally spaced between $t = 2$ and $t = 3$; r_p increases from top to bottom. Contours indicate density on the orbital plane in steps of a factor of 4; dashed lines show grit, solid lines show gas, with a heavier contour for $\rho = 1$. Half-tones indicate shocks.

2.1. First passages

Figs. 3 and 4 report on the first passages of all collisions. Here the contours represent density in the orbital plane, evaluated using SPH-style interpolation; dashed contours show grit density, while solid contours show gas density. Shaded areas show where $\dot{u}_v > 0$; these track the shocks propagating through the gas.

The most obvious differences between the gas and grit models occur in the head-on collisions (top rows of Figs. 3 and 4). In the equal-mass head-on collision the two grit polytropes pass directly through each other. As they do so they are briefly compressed by their mutual gravity; at later times they rebound, spraying grit particles onto loosely-bound orbits, and fall back to form a single merged object (van Albada & van Gorkom 1977). The gas polytropes obviously

can't interpenetrate; a shock develops when they first touch. Subsequently the shocked gas forms a disk perpendicular to the collision axis and bounded on the left and right by strong shocks. In the final image of this collision (upper right in Fig. 3) no trace of the two gas polytropes remains; the shocked gas forms a single object which expands due to its large thermal energy content. On the other hand, the grit polytropes, having passed through each other, are still distinct.

The unequal-mass head-on collision produces a more complex morphology. As the small grit polytrope plunges through its larger partner it generates a “wake” – a region of higher density where gravitational focusing concentrates grit from the large polytrope towards the collision axis. This wake is similar to the mutual compression of the two grit polytropes in the equal-mass collision; in both cases the energy needed is extracted from orbital motion, resulting in rapid orbit decay. The gas model produces a very different result; as the small polytrope plows into its partner it creates a strong bow shock. This shock pushes gas *away* from the collision axis, evacuating a cavity in the wake of the small gas polytrope. Meanwhile, a weaker shock travels backward through the small polytrope. By the last image (upper right in Fig. 4) the bow shock has reached the surface of the large polytrope, while the cavity has been filled in; the small gas polytrope has lost most of its forward momentum and lies, still largely intact, near center of the combined object. In contrast, at this time the grit polytropes have temporarily separated, though they will soon fall back together.

Many of the dynamical effects just described also play a role in the off-axis collisions. In the equal-mass $r_p = 0.5$ collision the bodies of the two gas polytropes are traversed by parallel shocks which slow their relative motion and increase their entropy. The unequal-mass version of this collision produces an asymmetric bow shock as the small polytrope moves through the outer layers of its companion, leaving a temporarily furrow behind. In contrast, the grit versions of these collisions again show regions of enhanced density in the wakes of the interpenetrating polytropes. Less dramatic effects are seen in the wide collisions; the $r_p = 1$ collisions are basically “kinder and gentler” versions of their closer counterparts, with weaker shocks and more subtle wakes. Finally, the grazing collisions ($r_p = 1.5$), shown at the bottom of Figs. 3 and 4, don't develop significant shocks; these passages involve only gravitational interactions.

2.2. Orbit decay

Although their initial orbits are parabolic, all of the off-center collisions leave the participants on bound orbits after their first passage. This orbit decay is generally due to the transfer of orbital energy to internal degrees of freedom, but the way this transfer takes place may be quite different in gas and grit models.

From Fig. 2 it's already clear that the interplay between gravity and gas-dynamics in orbit decay is complex. The plots of $U(t)$ for the collisions with $r_p = 0.5$ and 1.0 show two or more minima, each representing a different pericentric passage. In three of these collisions the grit models return to pericenter *before* the corresponding gas models, but the *opposite* order is seen in the $(M_1/M_2, r_p) = (2, 0.5)$ collision. Thus compared to the grit models, gas can either accelerate or delay orbit decay.

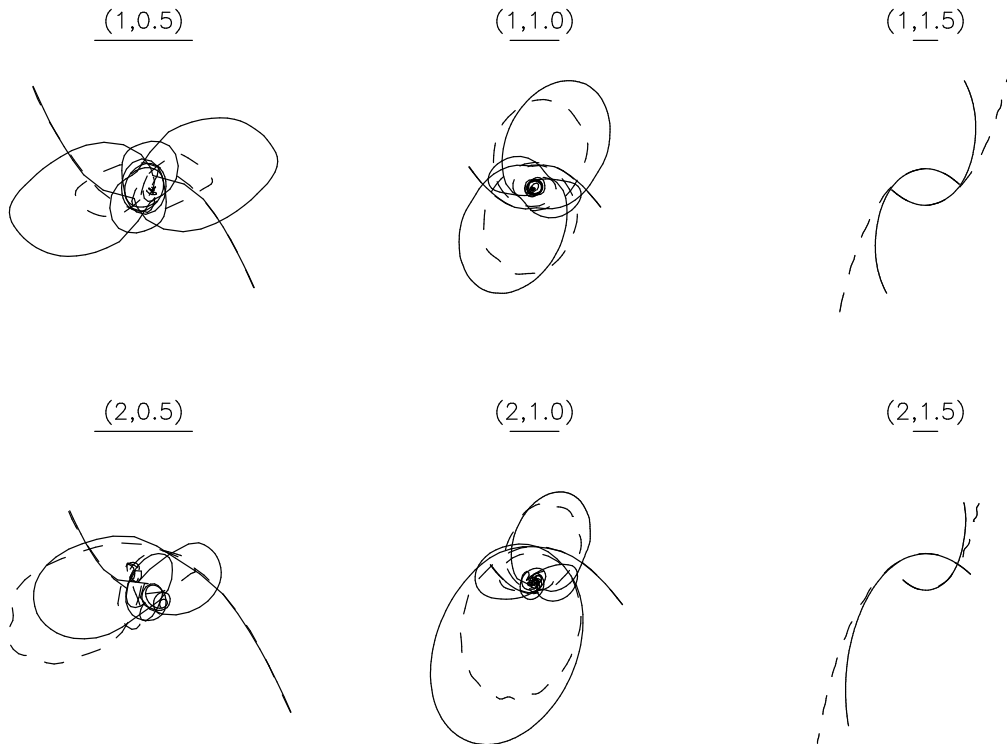


Figure 5. Orbital trajectories for all off-center collisions. Solid lines are gas results, while dashed lines are grit results. Each is labeled by $(M_1/M_2, r_p)$; the scale bar under each label is 1 unit long.

Fig. 5 shows orbital trajectories for all off-center collisions. These trajectories confirm that in the $(M_1/M_2, r_p) = (1, 0.5)$, $(1, 1.0)$, and $(2, 1.0)$ collisions the grit models undergo more rapid orbit decay than their gas counterparts, and that the opposite is true for the $(2, 0.5)$ collision. Moreover, they reveal a further puzzle; in grazing collisions the outgoing orbits of the gas polytropes are more tightly bound than those of their grit doppelgangers.

Closer inspection of Fig. 5 suggests a mechanism which might delay orbit decay in some gas models. Collision $(M_1/M_2, r_p) = (1, 0.5)$, in which the difference between the gas and grit models is quite dramatic, shows it most clearly: on their first passage the gas polytropes “bounce” off each other as if elastic. Of course, this is not too surprising; an ideal gas is *perfectly* elastic in the absence of shocks. Moreover, the corresponding panel of Fig. 2 shows a sharp peak in the thermal energy $T(t)$ during this passage, and Fig. 3 shows that the gas is compressed to roughly twice its initial density at the moment of closest approach ($t \simeq 2.5$). Similar bouncing trajectories are seen in the other off-axis collisions.

On the other hand, the rapid orbit decay of the $(M_1/M_2, r_p) = (2, 0.5)$ collision points to a different effect. Here as in the head-on cases the orbits of the gas polytropes decay faster than the orbits of their grit counterparts. For the head-on collisions this is no great mystery; ram pressure brings the

gas polytropes to a screeching halt on their first and only passage. A similar explanation probably applies in this deeply-penetrating off-axis collision; the small polytrope does so much work plowing through the body of its large partner that it loses most of its orbital momentum.

The puzzle of the grazing collisions can't be explained in this way as the gas polytropes barely touch each other. These decays are governed by tides, and it may seem paradoxical that the gas and grit models with $r_p = 1.5$ diverge since the same tidal gradients exist in both cases. However, the bottom rows of Figs. 3 and 4 show that gas polytropes suffer stronger tidal distortions in grazing collisions than do their grit counterparts. This makes sense; in the initial polytropes, gas particles are nearly stationary, while grit particles are in constant motion. Thus during a tidal encounter, a well-placed gas particle can accumulate more momentum than a wandering grit particle. Now the stronger tidal response of the gas polytropes is the key; recall that there would be *no* orbit decay whatsoever if both participants remained exactly spherical. By being more responsive, gas polytropes couple orbital motion to internal degrees of freedom more effectively, and hence in grazing collisions their orbits decay faster than those of grit polytropes.

2.3. Later passages

Thanks to orbit decay, later passages are slower and closer than first ones. Closer passages are always more violent, as Figs. 3 and 4 amply illustrate. On the other hand, the speed of passage affects gas and grit models in different ways. For grit models, slower passages are generally *more* disruptive; galaxies collide in exactly the way that cars don't, because low speeds give tides more time to act. Gas models, though also sensitive to tides, suffer less from shocks in slow collisions; the coalescence of two gas polytropes is more like a gentle swirling together than a head-long plunge.

Every passage pumps orbital energy into internal degrees of freedom, distending both gas and grit polytropes. After each passage, gas systems relax into convectively stable configurations; low-entropy material remains centrally concentrated, while high-entropy material forms an extended envelope. Grit systems also acquire distended outer envelopes; eq. 5 conserves phase-space density, so in phase-space such an envelope is really a thin "hyper-ribbon", tidally extracted from the main body, which still has the high phase-space density of its source. Nonetheless, this ribbon comes to resemble a smooth envelope as phase-mixing winds it into a tight spiral.

In basic outline, final encounters resemble mild versions of head-on collisions; either both partners are subsumed into a single object, or one partner burrows into the center of the other.

3. Remnant Structure

In the aftermath of a merger the wreckage undergoes a last episode of dynamical relaxation as it evolves towards an equilibrium configuration. This final convulsion generally begins at the center and travels outward. In a grit system potential fluctuations during the final merger scatter particles onto loosely-bound radial orbits; as these outgoing particles reach apocenter they create a caustic or

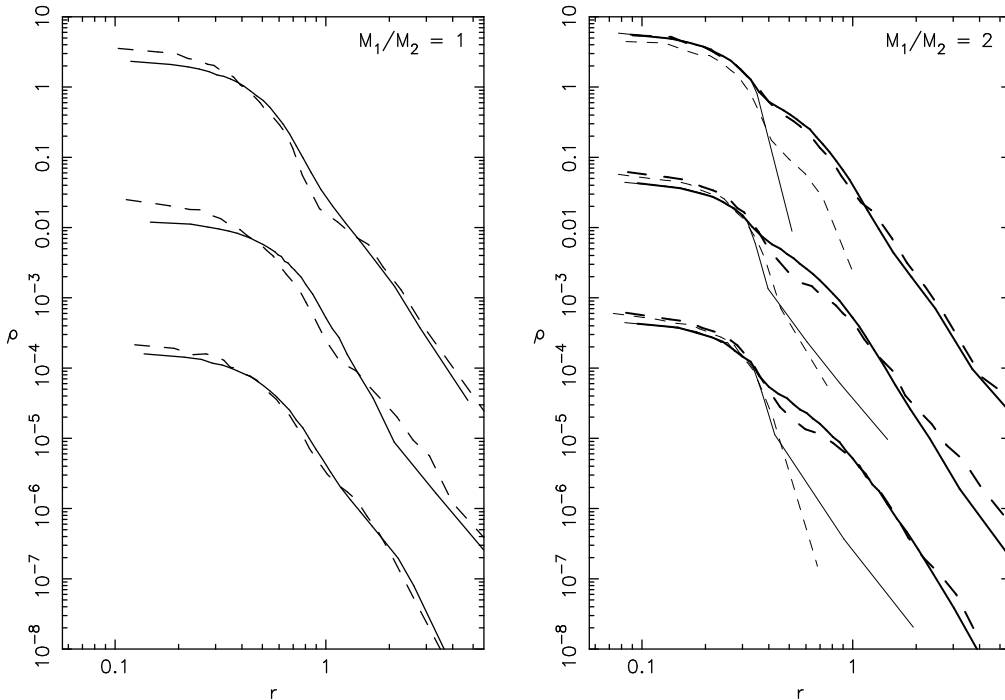


Figure 6. Density profiles derived by spherical averaging. Solid lines are gas results, while dashed lines are grit results. Left: remnants of equal-mass collisions. Right: remnants of unequal-mass collisions; thin lines show profiles for particles from the small polytropes. Top to bottom: remnants of collisions with $r_p = 0, 0.5,$ and $1,$ displaced downward by successive factors of 100 for clarity.

“shell”. In a gas system the final merger may create a weak outgoing shock, but much of the readjustment takes place at subsonic velocities, with no attendant increase in entropy.

3.1. Density profiles

Fig. 6 presents density profiles for all six merging collisions (those with $r_p \leq 1$). These profiles were calculated by evaluating the mass in nested spherical shells. Despite the differing dynamics of gas and grit mergers, the resulting remnants have similar profiles over a range of five decades in density. At large radii both grit and gas densities fall off roughly as $\rho \propto r^{-4}$. For grit models this asymptotic slope results as phase-mixing spreads out a population of particles with a wide range of energies including both bound and unbound orbits (Jaffe 1987; White 1987).

The unequal-mass mergers yield density profiles with “shoulders” where the slope briefly becomes shallower as r increases. These compound profiles arise because the small polytropes resist disruption during the merger process. The thin lines in the right-hand panel of Fig. 6 show density profiles derived using *only* particles originating in from the small polytropes. In every case, the small

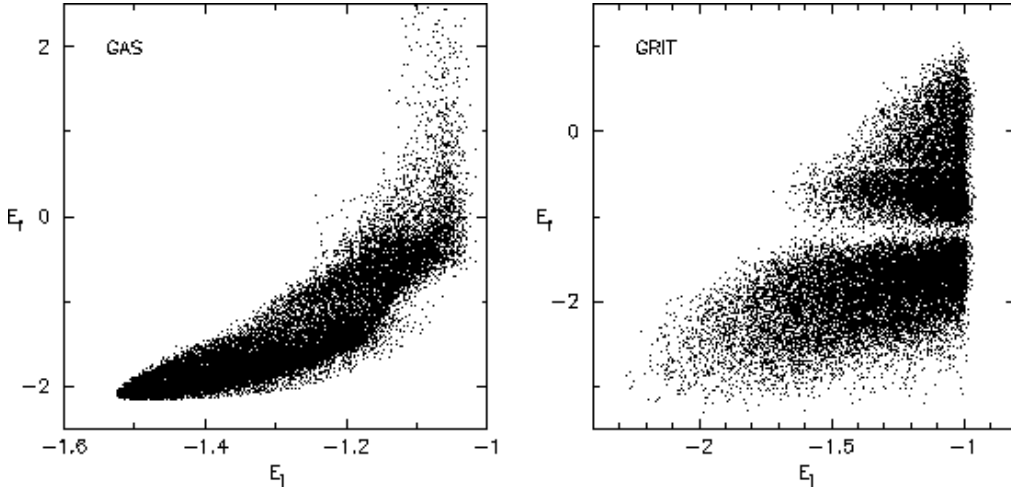


Figure 7. Initial vs. final binding energies for particles from remnants of $(M_1/M_2, r_p) = (1, 0.0)$ collision. Left: gas model; right: grit model. Note that the two plots have different scales. In both plots, $E = 0$ is escape energy.

polytropes have settled, virtually intact, in the centers of the merger remnants. For the gas models, this outcome is explained by the lower entropy which the small polytrope retains throughout the collision and merger; the remnant can't be convectively stable unless this low-entropy material winds up at the center.

If both partners have the *same* entropy, how much rearrangement takes place during a merger? Fig. 7 presents scatter-plots of initial binding energy E_i vs. final binding energy E_f for particles in both versions of the $(M_1/M_2, r_p) = (1, 0.0)$ collision. Here E_i was measured with the polytropes at infinite separation, while E_f was measured from the merger remnant; internal energies were included in calculating binding energies of gas particles. These plots show that initial binding energy is a useful, albeit imperfect, predictor of final binding energy. For the gas model, the correlation between E_i and E_f is fairly strong; moreover, there is a one-to-one relationship between binding energy and radius, so the initial and final radii of gas particles are also correlated.

For the grit model things are more complex. As the right-hand panel of Fig. 7 shows, grit particles have a *bimodal* distribution of final binding energies. This arises because the orbital phases of individual grit particles have a strong bearing on their response to tidal interactions. For example, consider a particle which reaches an apocenter of its orbit just before the polytropes interpenetrate, and the subsequent pericenter just after they separate. Such a particle sees a deeper potential well while falling in than it does while climbing out, so it gains energy; conversely, a particle on a similar orbit with a different phase may lose energy. The resulting bimodal energy distribution explains the shoulder in the density profile of this remnant (Fig. 6, left-hand panel, upper dashed curve). Tightly-bound particles form the core, while the rest form the $\rho \propto r^{-4}$ envelope; the deficit of particles with $E_f \simeq -1.2$ accounts for the dip in $\rho(r)$ at $r \simeq 0.8$.

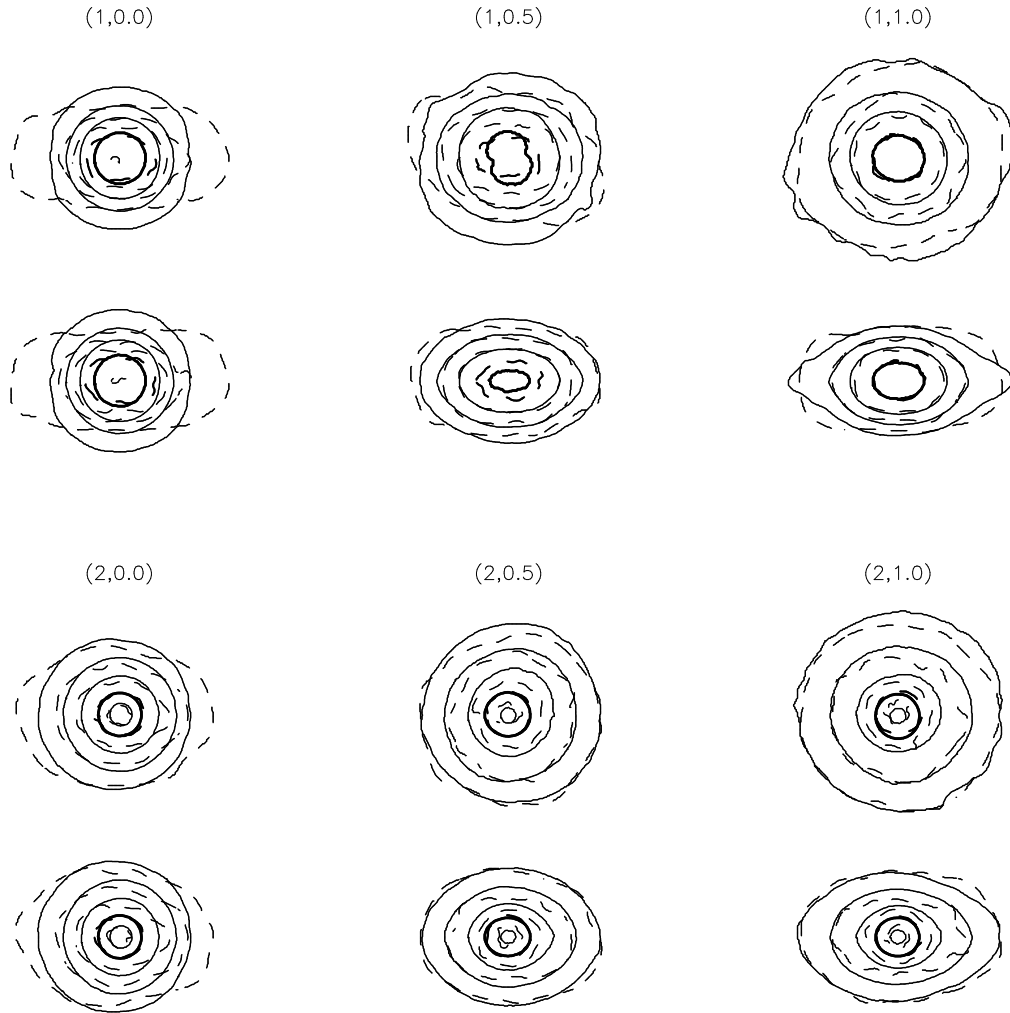


Figure 8. Merger remnants. Contours indicate densities in steps of a factor of 4; solid lines show gas, while dashed lines show grit. Each remnant is shown twice, once on a slice through the orbital plane (above), and once on a perpendicular slice (below).

3.2. Shapes

Fig. 8 presents density contours for the full sample of gas and grit merger remnants. Two slices through each remnant are shown; one slice in the orbital plane, and one slice at right angles to this plane. As in Figs. 3 and 4, here too the head-on collisions produce the most striking discrepancies between gas and grit models. The head-on gas remnants are nearly spherical, as expected for a self-gravitating gas configuration with no angular momentum. The head-on grit remnants, on the other hand, are prolate bars aligned with the collision axis. This is a “long-term” memory of the original collision velocities. Without the

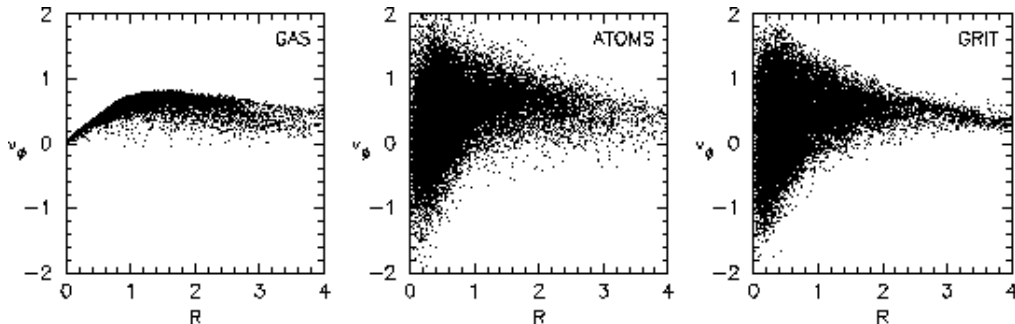


Figure 9. Rotation velocities v_ϕ vs. cylindrical radii R for remnants of $(M_1/M_2, r_p) = (1, 1.0)$ collision. Left: gas model; middle: gas atoms; right: grit model.

short-range interactions which randomize gas motions, grit systems maintain anisotropic velocity dispersions which can support such aspherical shapes.

The remnants produced in off-axis collisions have significant amounts of angular momentum. Most such collisions yield fairly oblate remnants; sliced perpendicular to the orbital plane, the gas remnants are sometimes “disky” while the grit remnants seem more “boxy”, but in general the density contours are very similar. The remnants formed by the $(M_1/M_2, r_p) = (1, 0.5)$ collisions are somewhat unusual in this regard. Both are distinctly non-axisymmetric; sliced along the orbital plane, the grit model has elliptical density contours at all radii, while the gas model seems to have a doubled core and a slightly elongated envelope. The grit remnant may be stable, since anisotropy and rotation together can support a tumbling triaxial structure in equilibrium. The same may not be true of the non-axisymmetric gas remnant; more experiments could help settle this issue.

3.3. Kinematics

Fig. 9 compares the kinematics of gas and grit versions of remnants from collision $(M_1/M_2, r_p) = (1, 1.0)$. This remnant has a relatively large amount of angular momentum and a major-to-minor axis ratio of roughly 2:1. Here the velocity in the direction of rotation, v_ϕ , has been plotted against cylindrical radius in the rotation plane, R . Between the plots of particle velocities for gas (left) and grit (right), an additional plot shows velocities of gas atoms taking thermal motion into account (middle). The gas has a very regular velocity field, as reported in previous studies (eg. Lombardi, Rasio, & Shapiro 1996). In contrast, the grit has a broad distribution of velocities at each point; while the overall sense of rotation is the same as in the gas case, some grit particles even counter-rotate. But when the grit is compared to the gas *atoms*, it’s evident that these velocity distributions are very much alike. The similarity of these distributions is consistent with the good match between the density contours of the gas and grit versions of this remnant (Fig. 8, upper-right).

Kinematics for the remnants of the head-on collision $(M_1/M_2, r_p) = (1, 0.0)$ are presented in Fig. 10. Here the radial velocity, v_r , has been plotted against the

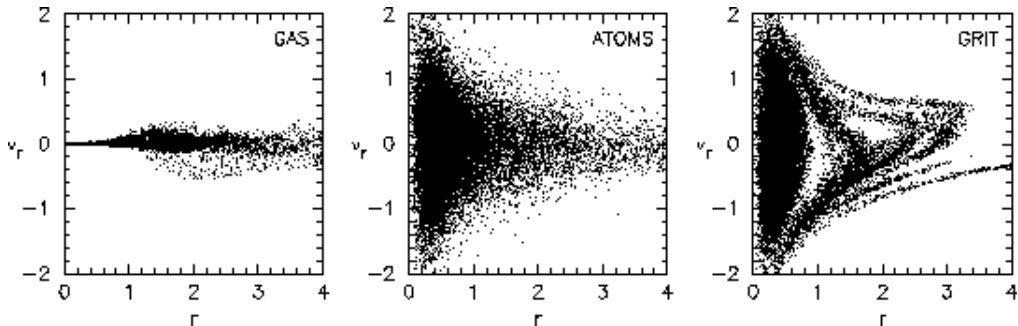


Figure 10. Radial velocities v_r vs. radii r for remnants of $(M_1/M_2, r_p) = (1, 0.0)$ collision. Left: gas model; middle: gas atoms; right: grit model.

spherical radius, r . This remnant has no angular momentum, so gas velocities should vanish; the small velocities seen in the left-hand panel indicate that the remnant is not yet fully relaxed. The grit version also is not yet completely relaxed, since in perfect equilibrium the distribution should be symmetric with respect to the line $v_r = 0$. Moreover, the grit plot shows that in phase-space the envelope of this remnant is not smooth, but consists of narrow ribbons of particles. These particles populate the upper peak in the final binding energy distribution for this remnant (Fig. 7, right-hand panel); launched as the two polytropes interpenetrated, they fell back in coherent streams and have since been wound up by ongoing phase-mixing. With time this fine structure will become harder to see, and eventually this plot will look something like the plot of atomic velocities shown in the middle. But even in the limit $t \rightarrow \infty$ some differences will remain; these include the radial anisotropy of the grit velocity distribution and bimodal nature of its binding energy distribution.

4. Conclusions

Comparison of gas-dynamical and stellar-dynamical models of colliding systems reveals many specific differences and hints at some underlying similarities. While stellar systems interact via gravity alone, gas systems interact via a complex mixture of gravity, pressure forces, and shocks. This mix greatly increases the range of dynamical behavior in stellar collisions. Even when interactions between gas systems are limited to tides, the resulting deformations are stronger than those seen in equivalent encounters of stellar systems.

Remnants of gas-dynamical and stellar-dynamical mergers also exhibit significant differences. Stellar systems have anisotropic velocity distributions, supporting a wide range of remnant morphologies, while gas systems settle into a small range of equilibria. But at the same time, the stellar and gaseous remnants studied here have very similar density profiles, and often similar shapes as well. This seems remarkable, since the physics behind these density profiles is rather different. The extended envelopes of gaseous remnants contain high-entropy material produced by shocks, which are violent, well-localized events resulting from physical encounters. On the other hand, the envelopes of stellar remnants con-

tain material extracted from the participants by tides; this material retains the high fine-grain phase-space density it starts with, and only when coarse-grained does it approximate the atomic velocity distribution of a gaseous envelope. Two puzzles remain: first, why do such disparate mechanisms – shocks and tides – produce such similar remnant envelopes? And second, how is coarse-graining – an operation applied to a stellar system by an observer – analogous to the irreversible physical processes which occur in gaseous systems?

Acknowledgments. I thank Piet Hut, James Lombardi, Frederic Rasio, and Stuart Shapiro for helpful suggestions. Support for this work was provided by NASA grant NAG 5-8393 and by Space Telescope Science Institute grant GO-06430.03-95A.

References

- Antonov, V. A. 1962, *Vestn. Leningrad Univ.*, 19, 96 [translated in de Zeeuw, T., ed. 1987, *Structure and Dynamics of Elliptical Galaxies* (Dordrecht: Reidel), p. 531]
- Barnes, J. E. 1998, *Galaxies: Interactions and Induced Star Formation*, eds. D. Friedli, L. Martinet, D. Pfenniger (Berlin: Springer-Verlag), 275
- Barnes, J., Goodman, J., Hut, P. 1986, *ApJ*, 300, 112
- Chandrasekhar, S. 1939, *An Introduction to the Study of Stellar Structure* (Chicago: Univ. of Chicago Press)
- Eddington, A. S. 1916, *MNRAS*, 76, 572
- Hénon, M. 1973, *A&A*, 24, 229
- Hernquist, L. 1993, *ApJ*, 404, 717
- Hernquist, L. & Katz, N. 1989, *ApJS*, 70, 419
- Jaffe, W. 1987, *Structure and Dynamics of Elliptical Galaxies*, ed. T. de Zeeuw (Dordrecht: Reidel), p. 511
- Kalnajs, A. 1972, *ApJ*, 175, 63
- Lacey, C. G., Ostriker, J. P. 1985, *ApJ*, 299, 633
- Lombardi, J. C., Rasio, F. A., Shapiro, S. L. 1996, *ApJ*, 468, 797
- Lynden-Bell, D. 1962, *MNRAS*, 124, 279
- Monaghan, J. J. 1992, *ARA&A*, 30, 543
- Monaghan, J. J., Gingold, R. A. 1983, *J. Comp. Phys.*, 52, 374
- Nelson, R. P., Papaloizou, J. C. B. 1993, *MNRAS*, 265, 905
- Nelson, R. P., Papaloizou, J. C. B. 1994, *MNRAS*, 270, 1
- Sills, A., Lombardi, J. C. 1997, *ApJ*, 484, L51
- Toomre, A. 1964, *ApJ*, 139, 1217
- van Albada, T. S., van Gorkom, J. H. 1977, *A&A*, 54, 121
- White, S. D. M. 1987, *Structure and Dynamics of Elliptical Galaxies*, ed. T. de Zeeuw (Dordrecht: Reidel), p. 339